


Article

# Hierarchically Ordered Macroporous–Mesoporous (HOM-m) MgFe<sub>2</sub>O<sub>4</sub>/MgO for Highly Efficient Adsorption of Ce(III) and La(III): Experimental Study and DFT Calculation Analysis

Lina Zhang <sup>1</sup>, Jiarui Lu <sup>2</sup> and Baixiong Liu <sup>2,\*</sup> 

<sup>1</sup> College of Intelligent Manufacturing, Gannan University of Science and Technology, Ganzhou 341001, China; linasuzhou@126.com

<sup>2</sup> College of Materials Science and Engineering, Jiangxi University of Science and Technology, Ganzhou 341001, China

\* Correspondence: liu\_micro@126.com

**Abstract:** This study employed a template method to prepare a highly ordered and interconnected porous HOM-m MgFe<sub>2</sub>O<sub>4</sub>/MgO rare earth ion-efficient adsorbent. The specific surface area of the adsorbent was as high as 130 m<sup>2</sup>/g, with saturation adsorption capacities for Ce(III) and La(III) of 5689.69 mg/g and 2123.50 mg/g, respectively. The adsorbent exhibited superparamagnetism with efficient and rapid separation from an aqueous solution using a magnet. The adsorption results indicated that the adsorption mechanism of HOM-m MgFe<sub>2</sub>O<sub>4</sub>/MgO towards Ce(III) and La(III) primarily involved the ion exchange and redox reactions between Mg(II) hydrolyzed from MgO and Ce(III)/La(III), as well as the electrostatic attraction between MgFe<sub>2</sub>O<sub>4</sub> and Ce(III)/La(III). Density functional theory (DFT) calculations revealed that the adsorption process was driven by the interaction of Ce(III) and La(III) ions with the surface oxygen atoms of MgFe<sub>2</sub>O<sub>4</sub>/MgO. Moreover, MgFe<sub>2</sub>O<sub>4</sub>/MgO showed a higher affinity and stronger adsorption effect towards Ce(III) than La(III). Adsorption cycling experiments demonstrated that even after three cycles, HOM-m MgFe<sub>2</sub>O<sub>4</sub>/MgO maintained good removal efficiency for Ce(III) and La(III). Therefore, this adsorbent shows promise as an effective material for removing Ce(III) and La(III) and has significant implications for the remediation of water resources in ion adsorption-type rare earth mining areas.

**Keywords:** rare earth ions; porous materials; magnetic adsorbents; adsorption mechanism



**Citation:** Zhang, L.; Lu, J.; Liu, B. Hierarchically Ordered Macroporous–Mesoporous (HOM-m) MgFe<sub>2</sub>O<sub>4</sub>/MgO for Highly Efficient Adsorption of Ce(III) and La(III): Experimental Study and DFT Calculation Analysis. *Separations* **2024**, *11*, 333. <https://doi.org/10.3390/separations11120333>

Academic Editors: Junlian Wang and Na Sui

Received: 24 October 2024

Revised: 16 November 2024

Accepted: 18 November 2024

Published: 21 November 2024



**Copyright:** © 2024 by the authors. Licensee MDPI, Basel, Switzerland. This article is an open access article distributed under the terms and conditions of the Creative Commons Attribution (CC BY) license (<https://creativecommons.org/licenses/by/4.0/>).

## 1. Introduction

Rare earth elements (REEs) are a group of chemical elements, which mainly consist of lanthanum (La), cerium (Ce), and another 15 lanthanide elements. Rare earth elements have exceptional physical and chemical qualities in areas such as optics, electronics, and magnetism and are widely sought globally [1,2]. They find extensive applications in areas such as new energy, national defense, and military technology, earning them the nickname “Vitamins of Modern Industry” [3,4]. Rare earth elements mostly exist as trivalent cations in ion-adsorption-type rare earth ores in regions such as Madagascar, Brazil, and the southern provinces of China [5]. Currently, in situ leaching technology is widely employed for the extraction of ion-adsorption-type rare earth ores [6]. In southern China, the primary method for extracting ion-adsorption-type rare earth ores involves leaching rare earth elements with ammonium sulfate solution, followed by precipitation with ammonium carbonate to obtain rare earth concentrates [7,8]. However, this process generates a large amount of low-concentration rare earth wastewater [9]. Additionally, under the long-term effects of rainfall, leachate from the mine migrates to adjacent water bodies, resulting in low-concentration rare earth wastewater pollution around the mine [10]. In recent decades, numerous studies have reported the significant threat to ecosystems and human

health [11–13]. Therefore, the treatment of wastewater containing low concentrations of rare earth ions is urgently needed.

Lanthanum (III) and cerium (III) are the two most abundant ones among rare earth elements and also the two most common rare earth elements in ion-adsorption rare earth ores. Thanks to their outstanding physical and chemical properties, they are widely applied in the fields of materials science, energy, and the electronics industry [14–16]. However, wastewater containing lanthanum elements generated during the extraction process can change the chemical properties of water bodies. In water, lanthanum ions may combine with anions (such as carbonate ions, phosphate ions, etc.), forming precipitates or complexes which can affect the growth of aquatic organisms. Wastewater containing cerium elements can be toxic to aquatic organisms and may even lead to the death of aquatic organisms, seriously affecting the ecological balance. Therefore, the removal of lanthanum (III) and cerium (III) from rare earth wastewater has also become a research hotspot among scholars both at home and abroad.

For example, Allahkarami et al. have comprehensively summarized the corresponding adsorption performance and adsorption mechanisms regarding the topic of using different adsorbents to remove cerium (III) from various aqueous solutions, providing an important reference basis for subsequent related research and practical operations [17]. Iftekhhar et al. focused on summarizing the influencing factors of different adsorbents on the adsorption of lanthanum (III), which can help people further understand and master the key points in the adsorption process so as to better carry out removal work [18]. All in all, being able to efficiently remove lanthanum (III) and cerium (III) from rare earth wastewater is of great significance for the sustainable development of the ecological environment.

In order to effectively recover and enrich low-concentration rare earth elements, methods such as precipitation [19], extraction [20], and adsorption [21] are widely used for leachate and wastewater generated from ion-adsorption-type rare earth ores. Among these methods, adsorption offers advantages such as simple operation, high treatment efficiency, and low processing costs, making it promising for the treatment of rare earth ion wastewater [22,23]. Currently, the materials used for rare earth ion adsorption mainly include activated carbon [24], metal oxides [25], natural zeolites [26], and clays [27]. However, due to their low saturation adsorption capacity, poor deep processing capability, and difficulty in separating them from water bodies, they reduce treatment efficiency and increase processing costs. Finding an adsorption material with a high saturation adsorption capacity, strong deep processing capability, and easy separation from water bodies is a direction of effort for many researchers.

In recent years, MgO has exhibited excellent adsorption performance, nontoxicity, alkalinity, and abundant surface-active sites, making it an efficient environmental adsorbent [28]. Previously, it has been demonstrated to be capable of removing heavy metals or dye molecules from wastewater [29–31]. In terms of heavy metal ion adsorption, MgO exhibits an excellent adsorption capacity for Pb(II) [32], Cd(II) [33], Ni(II) [34], As(III) [35], Cr(VI) [36], Se(IV) [37], and Se(VI) [38] because of its low price, fast adsorption rate, large saturation adsorption capacity, and strong deep processing capability. However, there have been no reports on the use of MgO as an adsorbent for rare earth ions. Therefore, this study investigated the adsorption of rare earth ions by MgO. Additionally, the literature indicates that the morphology, pore size, surface area, and surface defects of MgO significantly influence the performance of MgO adsorbents [39,40]. Increasing the specific surface area of nanomaterials is an effective method for enhancing the adsorption capacity of MgO nanomaterials. Ordered mesoporous materials have small pore sizes (2–50 nm) and large pore volumes; thus, preparing ordered mesoporous MgO can meet the requirement for high specific surface area of adsorbents [41]. However, because of the narrow pores, ions frequently collide with the pore walls during the adsorption process, significantly reducing the diffusion rate and mass transfer efficiency. On the other hand, macroporous materials (>50 nm) have lower probabilities of ion–pore wall collisions, resulting in higher mass transfer rates. Nevertheless, the pore quantity of macroporous materials is lower than that

of mesoporous materials, leading to a significant reduction in the specific surface area, which severely affects their adsorption performance. Therefore, employing macroporous materials as “high-speed lanes” to divide the elongated mesoporous “tunnels”, forming a high-speed mass transfer network, is an effective approach to address the low ion capture efficiency of ordered mesoporous MgO.

Centrifugal separation is frequently used after the adsorption of rare earth ions by adsorbents. However, centrifugal separation has low efficiency and significantly increases the cost of rare earth ion capture [42]. The preparation of adsorbents with ferromagnetic properties is a common method for achieving rapid and convenient separation of adsorbents from water. The magnetic portion of the synthesized magnetic adsorbents typically includes Fe [43],  $\text{Fe}_3\text{O}_4$  [44],  $\gamma\text{-Fe}_2\text{O}_3$  [45], and spinel ferrites ( $\text{MFe}_2\text{O}_4$ ), where M represents Mg, Mn, Co, Ni, Cu, etc.) [46,47]. Compared to other magnetic materials, the M(II) in  $\text{MFe}_2\text{O}_4$  is not sensitive to  $\text{O}_2$ ; hence, oxidation-reduction reactions are less likely to occur in air [48]. Therefore, creating an oxygen-free environment is not necessary during the preparation of  $\text{MFe}_2\text{O}_4$ , which makes the synthesis process simple and controllable.  $\text{MFe}_2\text{O}_4$  not only possesses excellent magnetism and biocompatibility but also has abundant hydroxyl groups (M-OH and Fe-OH) on the surface, serving as the main active sites for various ion binding activities.  $\text{MgFe}_2\text{O}_4/\text{MgO}$  can effectively alleviate the aggregation of magnetic entities in aqueous solutions and increase the adsorption sites of the adsorbent. Meanwhile, it can significantly reduce the cost of rare earth ion capture. Sun et al. constructed a  $\text{MgFe}_2\text{O}_4/\text{MgO}$  heterostructure to form oxygen vacancies for the adsorption of sulfamethoxazole (SMX) [49]. The heterostructure of  $\text{MgFe}_2\text{O}_4/\text{MgO}$  can generate a large number of vacancies at the interface, and these vacancies can serve as adsorption sites, enhancing the adsorption ability for target substances. Moreover,  $\text{MgFe}_2\text{O}_4$  and MgO each have different band structures. After the formation of the heterostructure, the interaction between them can lead to changes in the band structure. Such changes can make the material have selectivity for the adsorption of specific substances. Therefore,  $\text{MgFe}_2\text{O}_4/\text{MgO}$  has broad application prospects in the field of adsorption.

In this study, polystyrene (PS) microspheres were utilized as the macroporous hard template, and Pluronic F127 (poly(ethylene oxide)-poly(propylene oxide)-poly(ethylene oxide) triblock copolymer) served as the mesoporous soft template to prepare hierarchically ordered macroporous–mesoporous (HOM-m)  $\text{MgFe}_2\text{O}_4/\text{MgO}$  rare earth ion-efficient adsorbents for Ce(III) and La(III) adsorption. This method combines the high adsorption performance of MgO with the stable magnetism of  $\text{MgFe}_2\text{O}_4$  to synthesize an efficient and recyclable adsorbent for the adsorption of rare earth ions. Through isothermal adsorption, adsorption kinetics, and adsorption thermodynamics experiments, the adsorption behavior of HOM-m  $\text{MgFe}_2\text{O}_4/\text{MgO}$  on Ce(III) and La(III) was analyzed, and the influence of the initial solution's pH value, adsorbent dosage,  $\text{NH}_4^+$  concentration, and coexisting cation concentration on the adsorption results was determined. X-ray Photoelectron Spectroscopy (XPS) technology and density functional theory (DFT) calculations were employed in the experiments to thoroughly analyze the adsorption mechanism of the HOM-m  $\text{MgFe}_2\text{O}_4/\text{MgO}$  adsorbents on Ce(III) and La(III).

## 2. Materials and Methods

### 2.1. Materials

The chemical information is included in Table S1.

### 2.2. Characterizations

Scanning electron microscopy (SEM; Zeiss Sigma 300, Carl Zeiss AG, Oberkochen, Germany) was used to examine the micromorphology and elemental distribution of the materials. The phase composition and structural details of the samples within the  $10\text{--}90^\circ$  ( $2\theta$ ) range were recorded by X-ray diffraction (XRD; SHIMADZU XRD-7000, Shimadzu Corporation, Kyoto City, Japan) under  $\text{CuK}\alpha$  radiation. The specific surface area, pore volume, and pore size distribution of the materials were determined using a Brunauer–

Emmett–Teller analyzer (Micromeritics ASAP 2020, Micromeritics, Norcross, GA, USA). A vibrating sample magnetometer (VSM; Lake Shore 7404, Lake Shore, Columbus City, OH, USA) was used to analyze the magnetic hysteresis curves of the magnetic samples. The concentrations of Ce(III) and La(III) in the solution were determined by inductively coupled plasma optical emission spectrometry (ICP-OES; Agilent 8800, Agilent Technologies Inc., Santa Clara, CA, USA). Using Al K $\alpha$  radiation (1486.6 eV), XPS (Thermo Scientific K-Alpha, Thermo Fisher Scientific, Waltham, MA, USA) was used to determine the elemental composition and chemical states.

### 2.3. Material Synthesis

The schematic diagram of the HOM-m MgFe<sub>2</sub>O<sub>4</sub>/MgO rare earth adsorbent prepared by the sacrificial template method is shown in Figure 1.

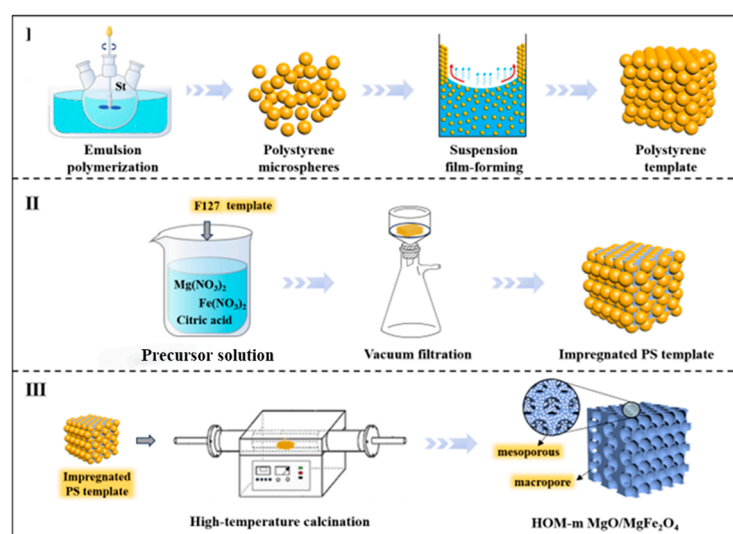


**Figure 1.** Scheme of HOM-m MgFe<sub>2</sub>O<sub>4</sub>/MgO prepared using colloidal crystal template method.

#### Step I: Preparation of polystyrene (PS) template

For the detailed experimental procedures, refer to the previous existing study [50]. Firstly, monodisperse polystyrene (PS) microspheres with a particle size of approximately 600 nm were synthesized using soap-free emulsion polymerization. Subsequently, the polystyrene colloidal crystal template was prepared using a constant-temperature suspension film-forming process. For detailed experimental procedures, please refer to Text S1 in the Supporting Information section.

#### Step II: Preparation of impregnated PS template

To prepare the impregnated PS template, 1.0 g of Pluronic F127 was dissolved in 10 mL of a 40% ethanol solution at room temperature and stirred to form colorless and transparent solution A. Solution B was made by dissolving 2.57 g of Mg(NO<sub>3</sub>)<sub>2</sub>·6H<sub>2</sub>O, 4.04 g of Fe(NO<sub>3</sub>)<sub>3</sub>·6H<sub>2</sub>O, and 2.10 g of citric acid containing 40% methanol and 60% ethylene glycol. Finally, solution A was mixed with solution B under magnetic stirring to prepare the precursor solution. The precursor solution was poured into a Buchner funnel containing 2.0 g of the PS colloidal crystal template, ensuring complete penetration of the liquid into the template to obtain the impregnated PS template.

#### Step III: Preparation of HOM-m MgFe<sub>2</sub>O<sub>4</sub>/MgO

Then, we dried the infiltrated PS template in an air atmosphere with a humidity lower than 40% for 48 h. Then, the dried template was placed in a tube furnace under an air atmosphere. It was heated from room temperature to 300 °C at a heating rate of 1.0 °C/min and kept for 180 min. After that, it was further heated up to 550 °C and

maintained for 300 min. Finally, the mixture was cooled to room temperature to obtain the HOM-m-MgFe<sub>2</sub>O<sub>4</sub>/MgO material.

#### 2.4. Batch Adsorption Experiments

Batch adsorption experiments were conducted in a constant-temperature shaking incubator at 25 °C and 100 rpm to investigate the adsorption capacity of HOM-m MgFe<sub>2</sub>O<sub>4</sub>/MgO for Ce(III) and La(III). In the isothermal adsorption and adsorption thermodynamics experiments, 10 mg of the adsorbent was added to 20 mL of Ce(III) and La(III) solutions with different initial concentrations (100–5000 mg/L). Ce(III) and La(III) solutions were prepared using Ce(NO<sub>3</sub>)<sub>3</sub>·6H<sub>2</sub>O and La(NO<sub>3</sub>)<sub>3</sub>·6H<sub>2</sub>O, respectively. Adsorption kinetic experiments were conducted at time intervals of 1, 2, 5, 10, 30, 60, 120, and 360 min, with an initial concentration of 500 mg/L for both Ce(III) and La(III). Additionally, a single-factor experiment was carried out to investigate the influence of different initial pH values (3–9), adsorbent dosages (5–25 mg), NH<sub>4</sub><sup>+</sup> concentrations (0–300 mg/L), and common coexisting cation concentrations (Mg<sup>2+</sup>, Ca<sup>2+</sup>, Al<sup>3+</sup>, Fe<sup>3+</sup>) on the adsorption of Ce(III) and La(III). After adsorption equilibrium was reached, the residual concentrations of Ce(III) and La(III) were measured using ICP. The equilibrium adsorption capacity and removal efficiency were calculated using Equations (1) and (2).

$$q_e = \frac{(C_0 - C_e)V}{m} \quad (1)$$

$$R = \frac{C_0 - C_e}{C_0} \times 100\% \quad (2)$$

where  $q_e$  represents the adsorption capacity of Ce(III) or La(III) at equilibrium (mg/g) and  $R$  is the removal efficiency of Ce(III) or La(III) (mg/g).  $C_0$  and  $C_e$  are the initial and equilibrium concentrations of the solution, respectively, measured in milligrams per liter.  $V$  represents the volume of the solution (liters) and  $m$  is the mass of the adsorbent (g).

Three parallel experiments were performed for each factor to confirm the authenticity and quality of the experimental data throughout the optimization of the adsorption trials. Detailed data analyses, including the kinetic and isotherm models, are presented in Table S2.

#### 2.5. Density Functional Theory (DFT) Calculations

Electronic structure calculations were performed using density functional theory (DFT), and all computations were implemented in Materials Studio with the CASTEP code. The Perdew–Burke–Ernzerhof (PBE) functional within the framework of the generalized gradient approximation (GGA) was employed to calculate the exchange correlation energy. Convergence criteria for energy change, maximum force, and maximum displacement were set at  $2 \times 10^{-5}$  eV/atom, 0.05 eV/Å, and 0.002 Å, respectively. To construct the adsorption models, the (100) and (311) crystal planes were sliced from the MgO and MgFe<sub>2</sub>O<sub>4</sub> crystals to form heterostructures. All atomic layers were placed on the xy-plane under periodic boundary conditions and with an additional vacuum layer of approximately 15 Å added in the direction perpendicular to the surface to eliminate interlayer interactions. Using the MgFe<sub>2</sub>O<sub>4</sub>/MgO heterostructure as the adsorbent and Ce(III) and La(III) as the adsorbates, the adsorption energies were calculated as follows:

$$E_{\text{ads}} = E_{\text{system}} - E_{\text{adsorbate}} - E_{\text{adsorbent}} \quad (3)$$

where  $E_{\text{system}}$ ,  $E_{\text{adsorbate}}$ , and  $E_{\text{adsorbent}}$  represent the optimized total energies (eV) of the adsorption system, adsorbate, and adsorbent, respectively. To investigate the interactions between Ce(III)/La(III) and MgFe<sub>2</sub>O<sub>4</sub>/MgO in more detail, we employed the charge density difference (CDD) and projected density of states (PDOS) to evaluate the interactions through electronic structure changes between the adsorbent and adsorbate.



### 3. Results and Discussion

#### 3.1. Structural Properties

The morphological characteristics of the absorbent samples were characterized by scanning electron microscopy (SEM). Figure 2a–d show SEM images of HOM-m  $\text{MgFe}_2\text{O}_4/\text{MgO}$  prepared by using polystyrene colloidal crystal templates with a particle size of approximately 600 nm as hard templates and the Pluronic F127 as a soft template. After calcination at 550 °C, the polystyrene colloidal crystal templates were eliminated while maintaining the structured pattern of the initial template. The final material had an ordered porous structure with large interconnecting pores separated by tiny window-like apertures. The macropores were organized in a structured manner with a consistent pore diameter of approximately 300 nm. This phenomenon is due to the fact both the template and pore walls contract simultaneously during calcination, leading to a shrinkage rate of approximately 50%. Surface imperfections in the macroporous material may be attributed to intrinsic flaws in the colloidal crystal template or the shrinking of pore diameters caused by uneven heating during calcination. In the magnified view of Figure 2d, the large pore walls are predominantly composed of  $\text{MgFe}_2\text{O}_4/\text{MgO}$  nanoparticles with a uniform distribution and an average particle size of approximately 20 nm. Additionally, numerous mesopores with sizes of approximately 10–20 nm were observed on the surface of  $\text{MgFe}_2\text{O}_4/\text{MgO}$ , which were attributed to the thermal decomposition of Pluronic F127 during calcination.

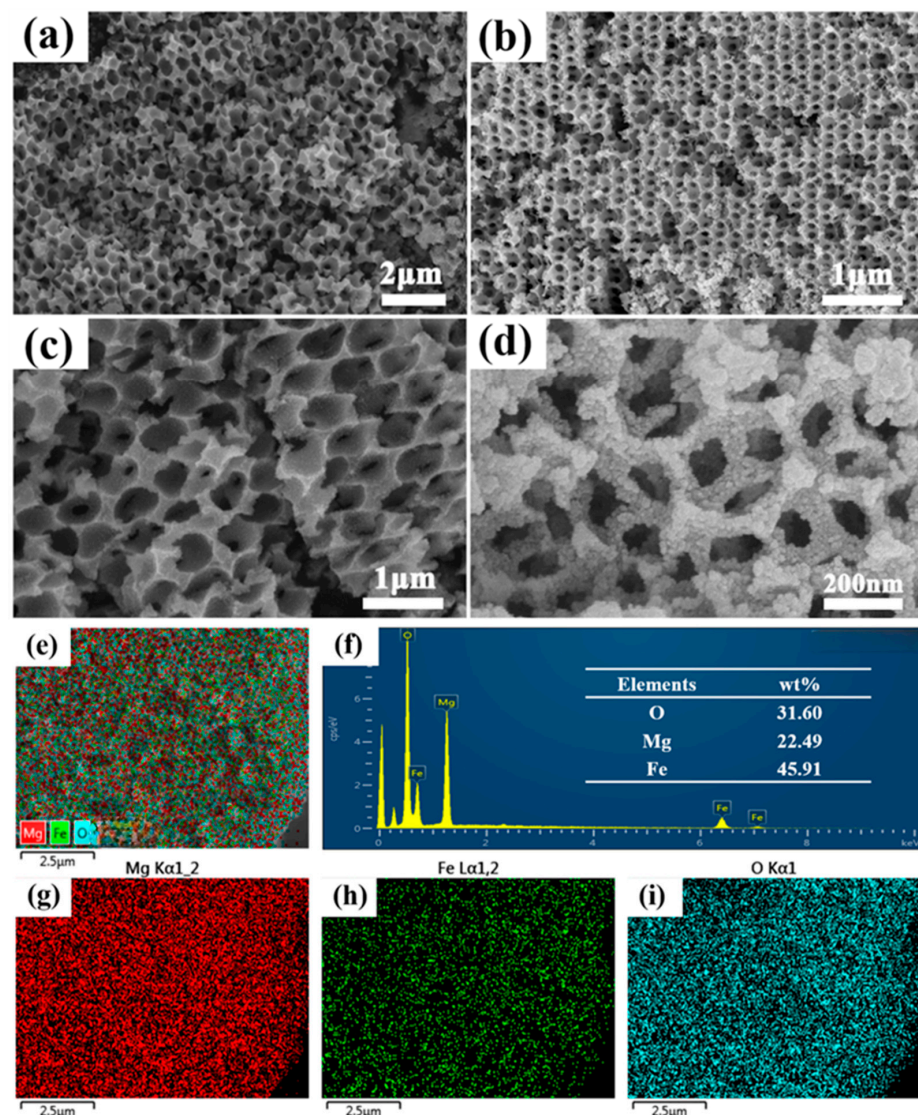
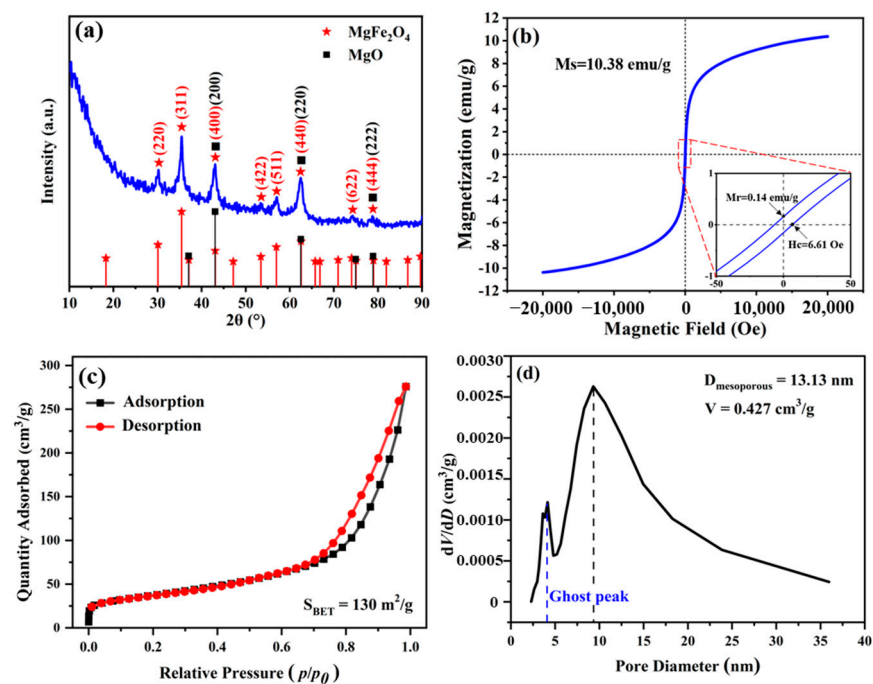


Figure 2. SEM images (a–d) and EDS element mappings (e–i) of HOM-m  $\text{MgFe}_2\text{O}_4/\text{MgO}$ .

Figure 2e–i present the EDS elemental mapping of the HOM-m  $\text{MgFe}_2\text{O}_4/\text{MgO}$ . Mg, Fe, and O were evenly distributed in the adsorbent material, confirming the presence of Fe in the form of composite oxides. Furthermore, elemental content analysis revealed an atomic ratio of Mg to Fe, which is consistent with the experimental design composition.

X-ray diffraction (XRD) analysis was performed on the adsorbent samples, and the results are shown in Figure 3a. The diffraction peaks at  $30.14^\circ$ ,  $35.45^\circ$ ,  $43.18^\circ$ ,  $57.09^\circ$ , and  $62.56^\circ$  correspond to the (220), (311), (400), (422) and (440) crystal planes of  $\text{MgFe}_2\text{O}_4$  (JCPDS 36-0398) [51,52]. The diffraction peaks at  $42.9^\circ$ ,  $62.3^\circ$ , and  $78.6^\circ$  correspond to the (200), (220) and (222) crystal planes of MgO (JCPDS 87-0653) [53,54]. The sharp and smooth baselines of the diffraction patterns indicated a high degree of crystallinity of the product. The absence of impurity peaks in the XRD spectrum confirms the formation of the  $\text{MgFe}_2\text{O}_4/\text{MgO}$  composite material. The Debye–Scherrer formula was applied to determine the particle size of the calcined product,  $D = k\lambda/(\beta \cos\theta)$  [55], where D represents the particle size, k is the Scherrer constant (0.89),  $\lambda$  is the X-ray wavelength (0.15406),  $\beta$  is the half-width of the diffraction peak, and  $\theta$  is the matching diffraction angle. In agreement with the findings of scanning electron microscopy (SEM), the particle size of HOM-m  $\text{MgFe}_2\text{O}_4/\text{MgO}$  was determined to be approximately 13.48 nm.



**Figure 3.** XRD patterns (a), magnetic hysteresis loops (b),  $\text{N}_2$  adsorption–desorption isotherms (c), and the corresponding pore size distributions (d) of HOM-m  $\text{MgFe}_2\text{O}_4/\text{MgO}$ .

Figure 3b shows the hysteresis loop of HOM-m  $\text{MgFe}_2\text{O}_4/\text{MgO}$  at a temperature of 298.15 K. The saturation magnetization ( $M_s$ ) is 10.38 emu/g, coercivity is 6.61 Oe, and remanence is 0.14 emu/g. The small coercivity and remanence indicate that HOM-m  $\text{MgFe}_2\text{O}_4/\text{MgO}$  exhibits superparamagnetic behavior.

The specific surface area, mesopore size, and pore volume of HOM-m  $\text{MgFe}_2\text{O}_4/\text{MgO}$  were characterized using  $\text{N}_2$  adsorption–desorption isotherms. The BET adsorption isotherm and the corresponding BJH pore size distribution curve are shown in Figure 3c,d. Please refer to Text S2 in the Supporting Information section for the calculation methods of pore size, pore volume and specific surface area. HOM-m  $\text{MgFe}_2\text{O}_4/\text{MgO}$  exhibited a typical Type II isotherm with a well-defined  $H_3$  hysteresis loop in the relative pressure range ( $P/P_0$ ) of 0.7–1.0, indicative of a macroporous material. No adsorption plateau was observed at  $P/P_0 \approx 1.0$ , and the  $H_3$  hysteresis loop is a characteristic feature of large-pore materials. The calculated specific surface area of HOM-m  $\text{MgFe}_2\text{O}_4/\text{MgO}$  was approximately  $130 \text{ m}^2/\text{g}$ .

From Figure 3d, it is evident that HOM-m MgFe<sub>2</sub>O<sub>4</sub>/MgO possesses abundant mesopores with a size range of approximately 5–20 nm, an average mesopore size of 13.13 nm, and a pore volume of approximately 0.427 cm<sup>3</sup>/g.

### 3.2. Adsorption Kinetics

The contact time is a crucial factor in assessing the rate of adsorption. The influence of contact time on the adsorption of Ce(III) and La(III) in wastewater by HOM-m MgFe<sub>2</sub>O<sub>4</sub>/MgO was studied, as shown in Figure 4a. It was observed that the adsorption rapidly increased within the first 30 min and reached equilibrium after 2 h. This might be attributed to the reduction in the concentration gradient of rare earth ions between the surface of MgFe<sub>2</sub>O<sub>4</sub>/MgO and the free rare earth ions, which leads to a decrease in the available adsorption active sites and an increase in the adsorption quantity.

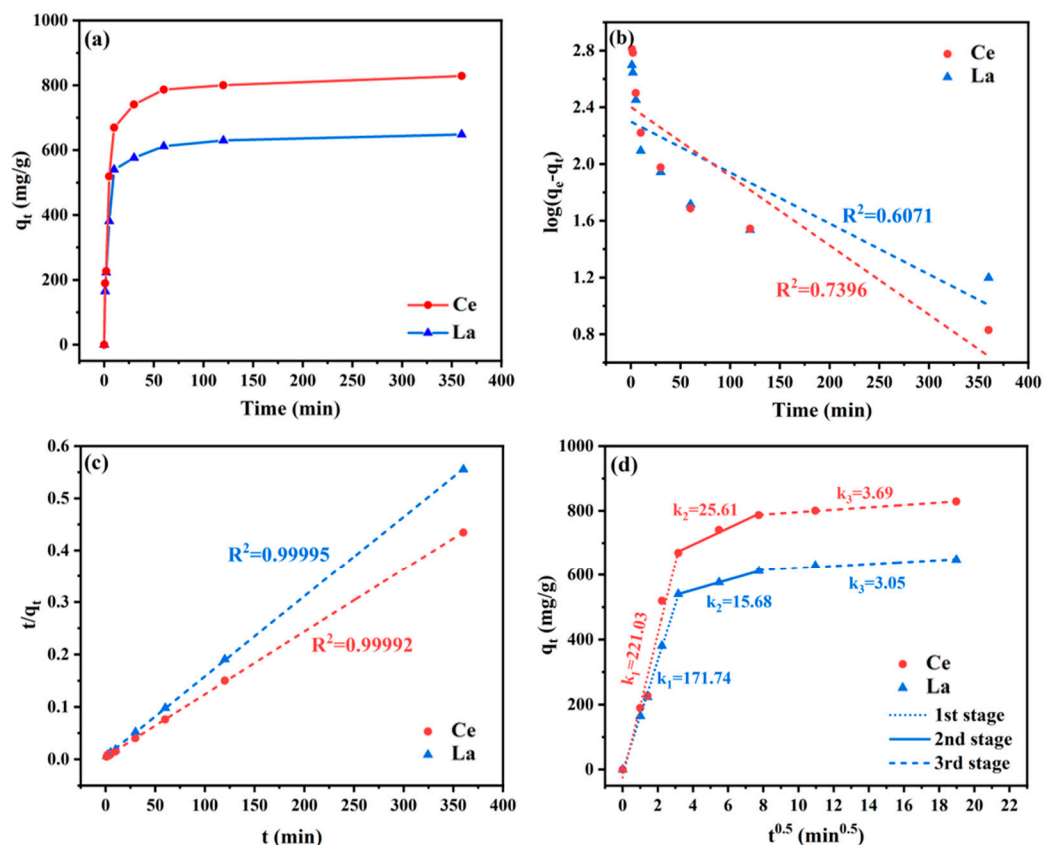


**Figure 4.** Kinetic curves of Ce(III) and La(III) of HOM-m MgFe<sub>2</sub>O<sub>4</sub>/MgO (a); the pseudo-first-order model fitting curves (b); pseudo-second-order model fitting curves (c); and the corresponding intra-particle diffusion plots (d).

To better understand the adsorption process and mechanism of HOM-m MgFe<sub>2</sub>O<sub>4</sub>/MgO for Ce(III) and La(III), we fitted the experimental results with the pseudo-first-order kinetic model (PFOM) (Figure 4b), pseudo-second-order kinetic model (PSOM) (Figure 4c), and intra-particle diffusion (DI) (Figure 4d) kinetic model. Tables S3–S5 show the fitted data. The results indicate that the PSOM fitting coefficients ( $R^2$ ) for the adsorption of Ce(III) and La(III) by the absorbent are closer to 1, and the calculated adsorption amounts ( $q_{e, cal}$ ) are close to the experimental adsorption amounts ( $q_{e, exp}$ ), suggesting that the adsorption system was mainly governed by chemical adsorption, such as ion exchange and complexation [56]. Additionally, the DI model displays three linear segments, indicating that the adsorption process of HOM-m MgFe<sub>2</sub>O<sub>4</sub>/MgO can be divided into three stages: surface diffusion, intraparticle diffusion, and adsorption–desorption equilibrium. During the first stage, Ce(III) and La(III) quickly move to the surface of the absorbent via ion exchange and electrostatic attraction, filling up external adsorption sites. During the second stage, the adsorption rate of the absorbent decreased until



it reached equilibrium. This may be attributed to the increased spread of Ce(III) and La(III) on the adsorbent surface into interior pores with fewer adsorption sites and narrower channels, which leads to a higher diffusion resistance and a decrease in the adsorption rate [57]. In the third step, the adsorbent reaches saturation. The adsorption kinetics findings indicate that the adsorption of Ce(III) and La(III) by HOM-m MgFe<sub>2</sub>O<sub>4</sub>/MgO involves a complicated, multistep process mostly driven by chemical adsorption.

### 3.3. Adsorption Isotherm

The adsorption isotherm describes the equilibrium relationship between the adsorbent and the adsorbed ions. The adsorption isotherms of HOM-m MgFe<sub>2</sub>O<sub>4</sub>/MgO for Ce(III) and La(III) at different initial concentrations at room temperature are shown in Figure 5a. The adsorption capacities of Ce(III) and La(III) exhibited a significantly increasing trend with variations in their initial concentrations. As the initial concentration increased, the rate of adsorption capacity enhancement slowed, ultimately reaching equilibrium. This phenomenon is attributed to the fact that, at low concentrations, the active sites of the adsorbent are sufficient to remove the target ions. However, as most active sites are occupied by Ce(III) and La(III), the diffusion of Ce(III) and La(III) from the liquid phase to the solid phase becomes increasingly challenging.

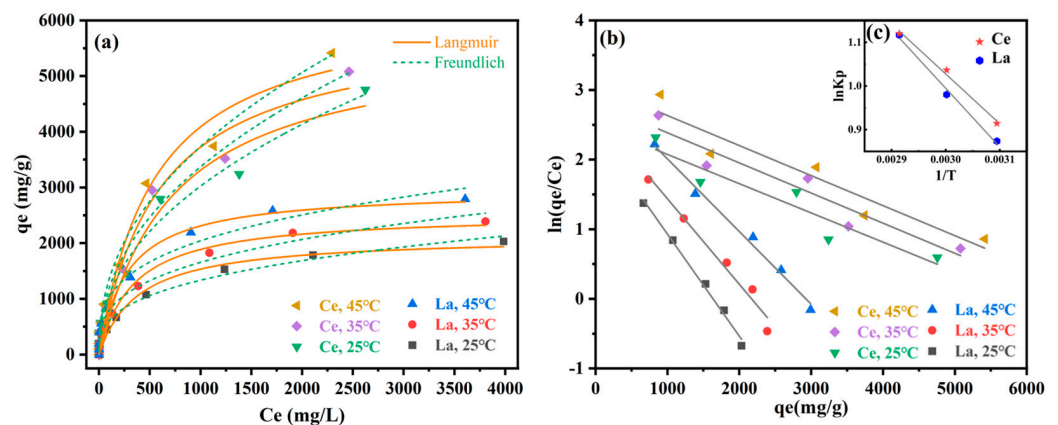


**Figure 5.** (a) Thermodynamic curves of Ce(III) and La(III) of HOM-m MgFe<sub>2</sub>O<sub>4</sub>/MgO; (b)  $\ln(q_e/C_e)$  with the linear fitting of  $q_e$ ; Inset (c) is  $\ln(K_p)$  with the linear fitting of  $1/T$ .

The adsorption isotherm data were analyzed by fitting the Langmuir and Freundlich models; the fitting results are presented in Table S6. It is evident that the fit coefficient  $R^2$  for the Freundlich model is closer to 1, indicating a better fit to the Freundlich model and a non-uniform adsorption process. Furthermore, the fit coefficient for the Langmuir model is close to 1, indicating that the adsorption process may involve uniform monolayer adsorption, possibly due to electrostatic attraction. The Freundlich fit results with  $1/n < 1$  and the Langmuir fit results with  $K_L$  values in the range of 0–1 suggest that the adsorption of Ce(III) and La(III) by HOM-m MgFe<sub>2</sub>O<sub>4</sub>/MgO is favorable [58]. According to the Langmuir fit results, the saturation adsorption capacities of HOM-m MgFe<sub>2</sub>O<sub>4</sub>/MgO for Ce(III) and La(III) are 5689.69 mg/g and 2123.50 mg/g, respectively.

### 3.4. Adsorption Thermodynamics

Temperature is also a crucial factor influencing adsorption. The adsorption isotherms of HOM-m MgFe<sub>2</sub>O<sub>4</sub>/MgO at different temperatures are shown in Figure 5a and the fitting results of the Langmuir and Freundlich models for the adsorption data are presented in Table S6. From the graph, it is evident that as the environmental temperature increases from 25 °C to 45 °C, the saturation adsorption capacity of the adsorbent for Ce(III) increases from 5689.69 mg/g to 6320.60 mg/g, and for La(III), it increases from 2123.50 mg/g to 2953.45 mg/g. The adsorption capacity increases with an increase in temperature.

The thermodynamic parameters for the adsorption of Ce(III) and La(III) by the adsorbent, such as entropy change ( $\Delta S^0$ ), enthalpy change ( $\Delta H^0$ ), and Gibbs free energy change ( $\Delta G^0$ ), were calculated, and the results are shown in Table S7. The equations for the calculation are as follows:

$$\Delta G^0 = -RT \ln K_p \tag{4}$$

$$\ln K_p = \frac{\Delta S^0}{R} - \frac{\Delta H^0}{RT} \tag{5}$$

where  $\Delta G^0$  is the standard Gibbs free energy of adsorption ( $\text{kJ}\cdot\text{mol}^{-1}$ ),  $R$  is the gas constant ( $8.314 \text{ J}\cdot\text{mol}^{-1}\cdot\text{K}^{-1}$ ),  $T$  is the adsorption temperature (K),  $K_p$  is the thermodynamic equilibrium constant determined by plotting  $\ln(q_e/C_e)$  against  $q_e$  (Figure 5b),  $\Delta S^0$  is the adsorption entropy change ( $\text{J}\cdot\text{mol}^{-1}\cdot\text{K}^{-1}$ ), and  $\Delta H^0$  is the adsorption enthalpy change ( $\text{kJ}\cdot\text{mol}^{-1}$ ).  $\Delta S^0$  and  $\Delta H^0$  were determined by plotting  $\ln K_p$  against  $1/T$  and obtaining the slope and intercept, respectively (Figure 5c).

According to the calculation results, negative values of  $\Delta G^0$  indicate that the adsorption of Ce(III) and La(III) is feasible and spontaneous. Additionally, the increasing magnitude of the negative  $\Delta G^0$  values with increasing temperature suggests that higher temperatures favor the adsorption of Ce(III) and La(III), mainly because the mobility of Ce(III) and La(III) increases with increasing temperature [59]. Furthermore, positive values of  $\Delta H^0$  and  $\Delta S^0$  indicate a decrease in the degree of freedom of the system during the adsorption process, suggesting a heat-absorbing and disorder-increasing adsorption process at the solid-solution interface [60].

### 3.5. Influence of Environmental Factors

HSC Chemistry (Ver.6.0) was used to simulate the potential and pH diagrams for Ce(III) and La(III) in the  $\text{H}_2\text{O}$  system (Figure 6). It was used to predict the stable forms and conditions of certain elements in aqueous solutions at specific potentials and pH values. The region between the oxygen line and the hydrogen lines represents the stability zone of  $\text{H}_2\text{O}$ . As shown in Figure 6a, the stable forms of Ce in the aqueous system are Ce(III),  $\text{CeO}^+$ , and  $\text{CeO}_2$ . Reactions (a), (b), and (c) correspond to Equations (6)–(8), respectively. As shown in Figure 6b, the stable forms of La in the aqueous system are La(III),  $\text{LaO}^+$ , and  $\text{La(OH)}_3$ . Reactions (d) and (e) correspond to Equations (9) and (10), respectively, with these reactions being pH-dependent and independent of the electrode potential.

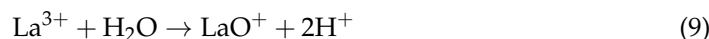
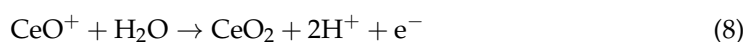
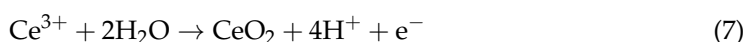
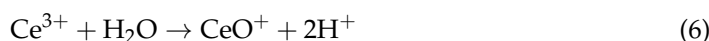
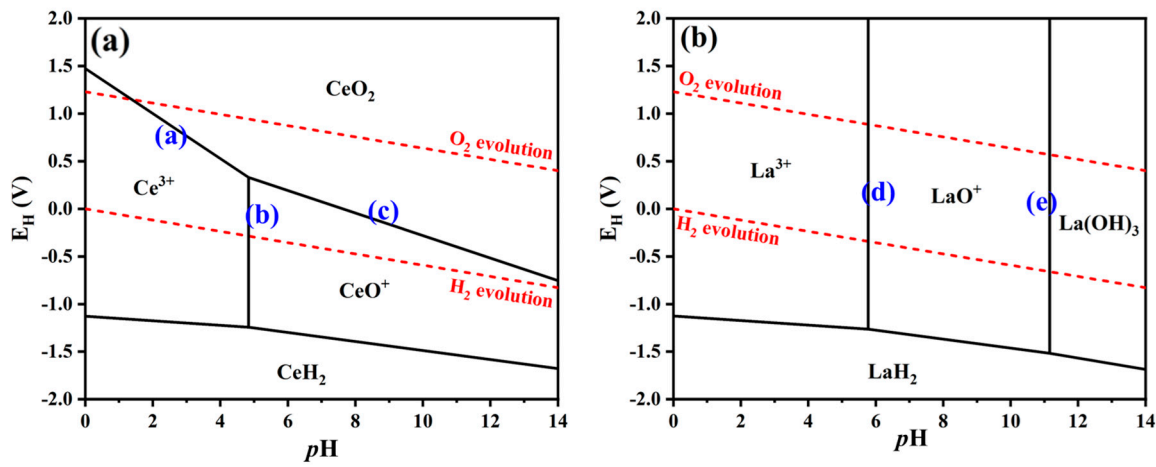
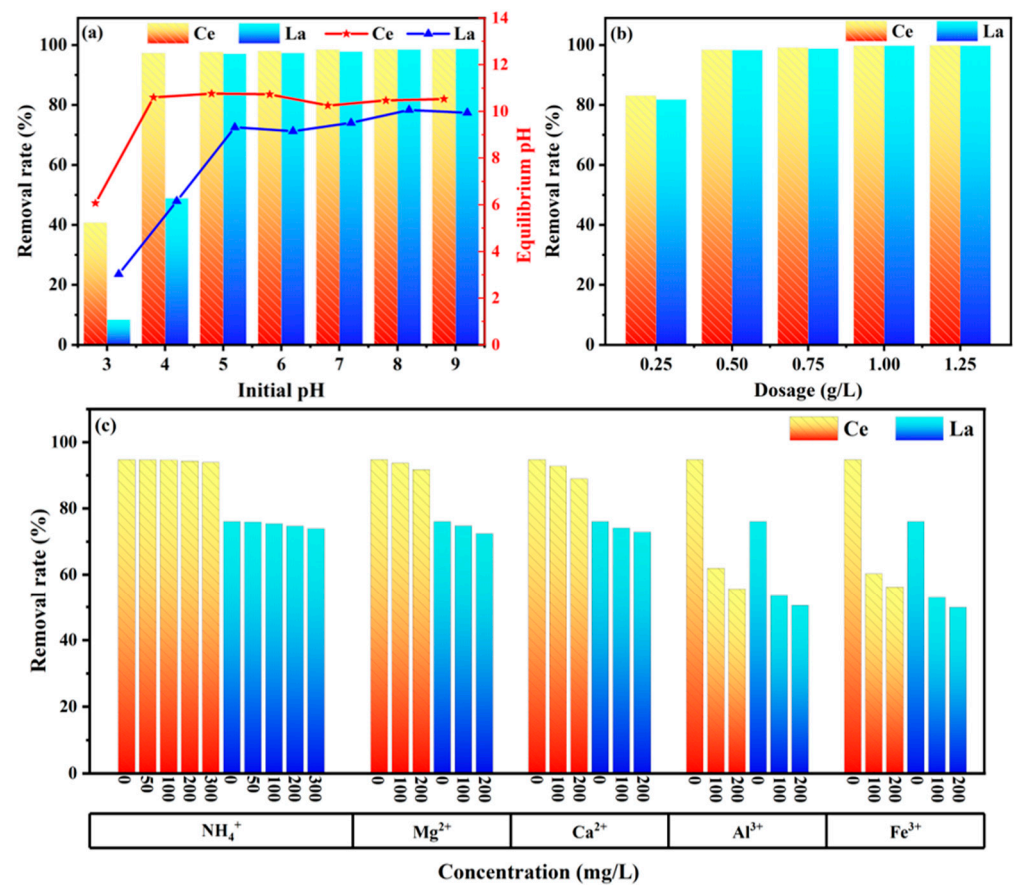


Figure 7a illustrates the influence of pH on the removal efficiency of Ce(III) and La(III) by the HOM-m  $\text{MgFe}_2\text{O}_4/\text{MgO}$ . Within the pH range of 3 to 4, the adsorption rate of La(III) by HOM-m  $\text{MgFe}_2\text{O}_4/\text{MgO}$  is low and increases with pH, stabilizing in the pH range of 5 to 9. The removal trend of Ce(III) is similar to that of La(III), with poor removal efficiency at pH = 3 and an increase followed by stabilization within the pH range of 4 to 9. This phenomenon arises from the competition between  $\text{H}^+$  and rare earth cations for adsorption sites at low pH, where  $\text{H}^+$  occupies the active sites of the adsorbent, leading to a lower removal efficiency. As the pH increases, the  $-\text{OH}$  groups on  $\text{MgFe}_2\text{O}_4$  and  $\text{MgO}$  ionize to  $-\text{O}^-$ , creating sufficient active sites that attract rare earth cations [61]. When  $\text{pH} > 7$ , rare earth cations gradually precipitate in the form of oxides and hydroxides, resulting in an insignificant removal efficiency. Additionally, the graph indicates a weaker pH effect on Ce(III) in low-pH environments, suggesting that HOM-m  $\text{MgFe}_2\text{O}_4/\text{MgO}$  exhibits strong resistance to pH interference during the adsorption process of Ce(III). The different

adsorption capacities of Ce(III) and La(III) may be attributed to variations in their affinities for HOM-m MgFe<sub>2</sub>O<sub>4</sub>/MgO.



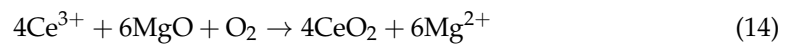
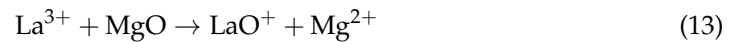
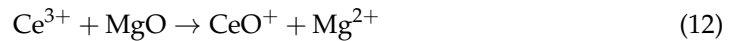
**Figure 6.** The relationship between the potential and pH of Ce(III) (a) and La(III) (b) in the H<sub>2</sub>O system.



**Figure 7.** The relationship between the removal rate of Ce(III) and La(III) and pH (a), dosage (b), and the concentrations of coexisting ions (c).

At an initial pH of 5–9, the pH values at equilibrium for Ce(III) and La(III) adsorption are approximately 10–11 and 9–10, respectively. The pH variation was mainly due to the reaction of MgO on the surface of MgFe<sub>2</sub>O<sub>4</sub>/MgO with H<sup>+</sup> in the solution (Equation (11)). Simultaneously, free Ce(III) and La(III) underwent hydrolysis to generate H<sup>+</sup> (Equations (6) and (9)), and free Ce(III) and La(III) were adsorbed on the MgFe<sub>2</sub>O<sub>4</sub>/MgO

surface through ion exchange with Mg(II) (Equations (12)–(15)). During the removal of Ce(III) and La(III), the equilibrium pH increased compared to the initial pH because of the decrease in H<sup>+</sup> production and the increase in H<sup>+</sup> consumption.



In the pH range of 5–7, the removal of Ce(III) and La(III) approaches 100%. Therefore, a pH of 5–7 was selected as the optimal adsorption environment. To eliminate interference from other ion forms of complexes and precipitates on the solubility of heavy metal ions and to ensure that rare earth ions play a primary role in the adsorption process, pH = 5–7 was chosen as the optimal pH for solutions containing Ce(III) and La(III). The pH values of the newly prepared Ce(III) and La(III) solutions were 5.83 and 5.58, respectively, requiring no pH adjustment and being able to be directly used for adsorption studies.

The influence of dosage on the removal efficiencies of Ce(III) and La(III) is depicted in Figure 7b. As the adsorbent dosage was increased, MgFe<sub>2</sub>O<sub>4</sub>/MgO provided more active sites, leading to an increase in the removal efficiency of Ce(III) and La(III). Beyond a dosage of 0.5 g/L, the growth rate of the removal efficiency for Ce(III) and La(III) by MgFe<sub>2</sub>O<sub>4</sub>/MgO gradually slowed, and the unit mass adsorption decreased. This phenomenon is attributed to the decreasing concentrations of Ce(III) and La(III) in the solution, resulting in a reduction in the adsorption driving force. Despite an increase in the number of active sites, equilibrium was eventually reached. Therefore, the optimum adsorbent dosage is determined to be 0.5 g/L for subsequent applications.

The effect of coexisting ion (NH<sub>4</sub><sup>+</sup>, Mg<sup>2+</sup>, Ca<sup>2+</sup>, Al<sup>3+</sup>, Fe<sup>3+</sup>) concentrations on the removal efficiency of Ce(III) and La(III) by HOM-m MgFe<sub>2</sub>O<sub>4</sub>/MgO is presented in Figure 7c. Owing to the significant production of ammonia–nitrogen in wastewater during rare earth resource extraction, it is essential to investigate the effect of ammonia–nitrogen concentration on the adsorption of Ce(III) and La(III). According to the experimental results, the adsorption of Ce(III) and La(III) is almost unaffected by NH<sub>4</sub><sup>+</sup>, possibly because monovalent ions have a lower charge density, making them interact more strongly with H<sub>2</sub>O than solid adsorbents [62]. Therefore, HOM-m MgFe<sub>2</sub>O<sub>4</sub>/MgO can be employed for the removal of Ce(III) and La(III) in ammonia–nitrogen environments. The influence of divalent ions (Ca<sup>2+</sup> and Mg<sup>2+</sup>) on the adsorption of Ce(III) and La(III) was smaller than that of trivalent ions (Al<sup>3+</sup> and Fe<sup>3+</sup>), indicating that trivalent ions were more competitive in the adsorption process of Ce(III) and La(III). This phenomenon is attributed to the higher affinity of trivalent ions compared to divalent ions for adsorption sites during the process of MgFe<sub>2</sub>O<sub>4</sub>/MgO adsorbing Ce(III) and La(III) [63].

### 3.6. Adsorption Mechanism Analysis

XPS was employed to examine the samples before and after the adsorption of Ce(III) and La(III), and the results are depicted in Figure 8. Figure 8a presents the full XPS spectrum of HOM-m MgFe<sub>2</sub>O<sub>4</sub>/MgO before and after adsorption, revealing that the Ce3d and La3d peaks increase after adsorption compared to the pre-adsorption state. The elemental composition changes on the surface of the adsorbent before and after the adsorption of Ce(III) and La(III) were analyzed using XPS survey spectra, as detailed in Table S8. After the adsorption of Ce(III) and La(III), the proportion of Mg notably decreased, while the variation in the proportion of Fe was minor. Conversely, the proportions of Ce and La increased, indicating successful adsorption of Ce and La onto the adsorbent.



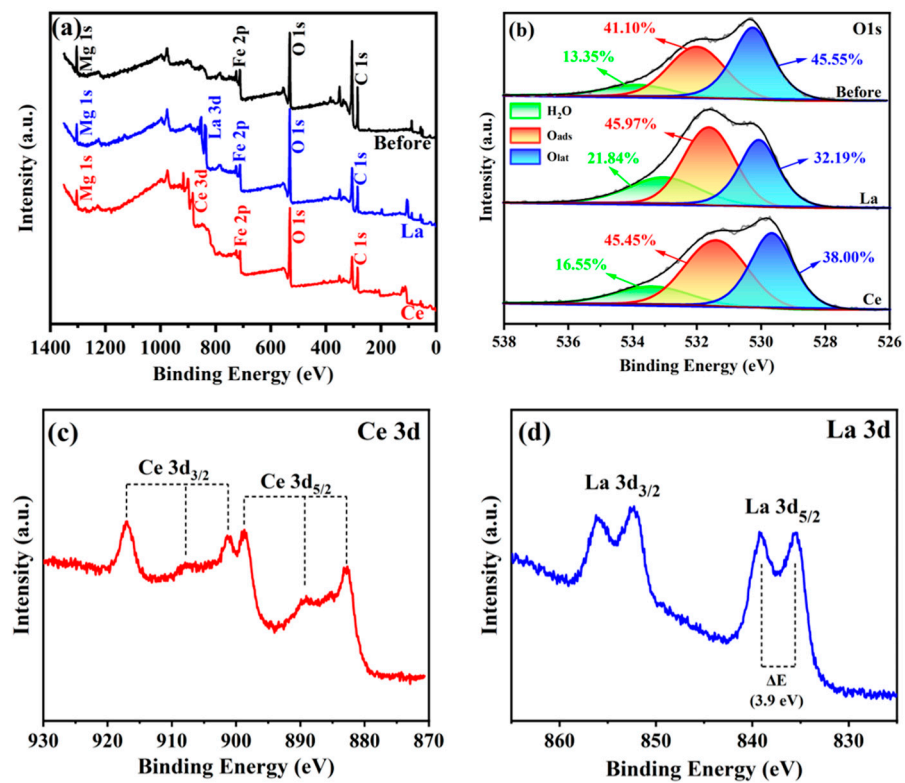


**Figure 8.** Full spectrum of XPS (a), O1s (b), Ce3d (c), and f La3d (d) of the adsorbent before and after adsorption of Ce(III) and La(III).

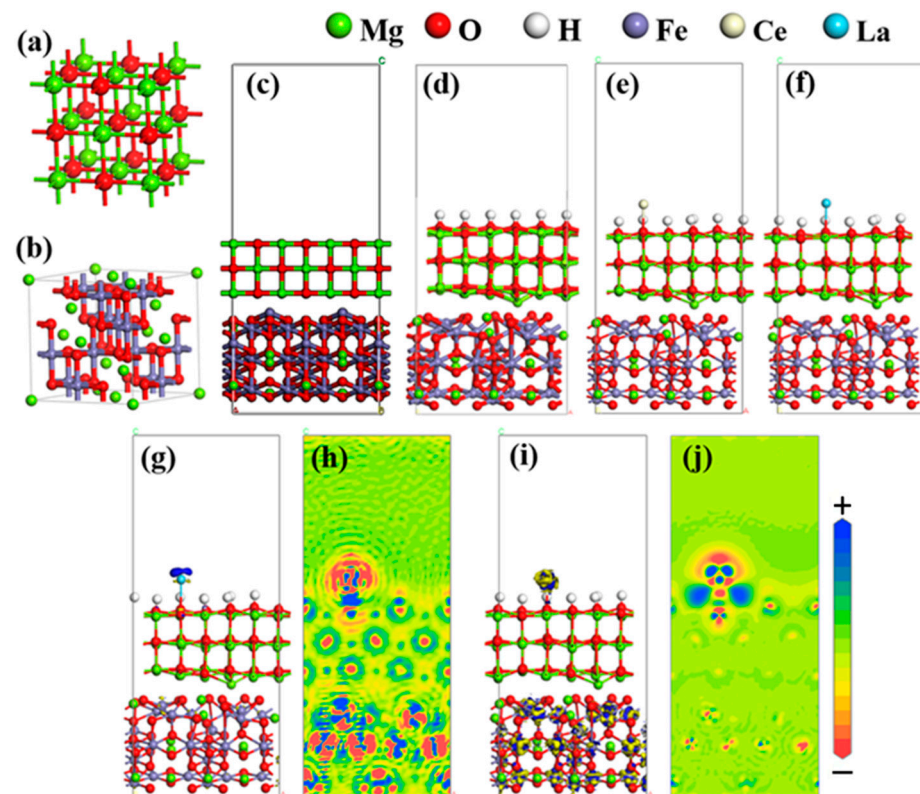
Figure 8c depicts the peak fitting of Ce3d, revealing two distinct spin–orbit split peaks at 882.93 eV and 901.22 eV corresponding to Ce 3d<sub>5/2</sub> and Ce 3d<sub>3/2</sub>, respectively, with 882.93 eV attributed to Ce–O, indicating the formation of cerium-containing compounds [64]. Each spin–orbit split peak further split into three multiple splitting peaks, totaling six visible peaks. Notably, the clear splitting peak at 916.98 eV suggests that the oxidation state of Ce is +4. Figure 8d shows the peak fitting of La3d, with two separated spin–orbit split peaks at 835.38 eV and 852.28 eV. These correspond to La 3d<sub>5/2</sub> and La 3d<sub>3/2</sub>, respectively, with 835.38 eV attributed to La–O, indicating the formation of lanthanum-containing compounds [65]. Each spin–orbit split peak further split into two multiple splitting peaks, totaling four visible peaks. The energy difference ( $\Delta E$ ) between the multiple splitting peaks for La 3d<sub>5/2</sub> is 3.9 eV, suggesting that the compound is La(OH)<sub>3</sub>.

Figure 8b presents the O1s peak fitting of HOM-m MgFe<sub>2</sub>O<sub>4</sub>/MgO before and after the adsorption of Ce(III) and La(III). Before adsorption, O1s can be divided into three peaks at 530.26 eV, 532.00 eV, and 533.85 eV, representing lattice oxygen (Mg–O, Fe–O), surface-adsorbed -OH (Mg–OH), and adsorbed water (H<sub>2</sub>O), respectively [66,67]. After La(III) adsorption, the lattice oxygen content on the surface of the adsorbent decreased from 45.55% to 32.19%, indicating a reduction in Mg–O. The adsorbed oxygen content increased from 41.10% to 45.97%, reflecting an increase in Mg–OH and La–OH. This was attributed to the hydrolysis of MgO and ion exchange with La(III) to form La(OH)<sub>3</sub>, indicating a chemical adsorption process. Following the adsorption of Ce(III), the lattice oxygen content on the surface of the adsorbent decreased from 45.55% to 38.00%, indicating a reduction in Mg–O. The adsorbed oxygen content increased from 41.10% to 45.45%, indicating an increase in Mg–OH. However, compared with the adsorption results for La(III), the transformation from lattice oxygen to adsorbed oxygen was relatively less pronounced after the adsorption of Ce(III). This is due to the redox reaction between MgO and Ce(III) ions, ultimately forming CeO<sub>2</sub>, which belongs to lattice oxygen. This adsorption process was also characterized by chemical adsorption.



### 3.7. DFT Calculation for Adsorption Mechanism

To further explore the adsorption mechanisms of  $\text{MgFe}_2\text{O}_4/\text{MgO}$  for  $\text{Ce(III)}$  and  $\text{La(III)}$ , density functional theory (DFT) calculations were employed to provide electronic-level evidence. Based on batch experiments and characterization results,  $\text{MgFe}_2\text{O}_4/\text{MgO}$  played a crucial role in the adsorption of  $\text{Ce(III)}$  and  $\text{La(III)}$ . Therefore, calculations were conducted by constructing  $\text{MgFe}_2\text{O}_4/\text{MgO}$  heterostructures (Figure 9c) and optimizing their initial configurations (Figure 9d). Because the adsorption process occurs in aqueous solutions,  $\text{MgO}$  surface hydrolysis leads to partial oxygen atom hydroxylation, resulting in the incorporation of a small number of hydroxyl groups in the structure. Figure 9e,f depicts the structural diagrams of  $\text{MgFe}_2\text{O}_4/\text{MgO}$  adsorbing  $\text{Ce(III)}$  and  $\text{La(III)}$ , respectively. Both  $\text{Ce(III)}$  and  $\text{La(III)}$  are positioned above the O atoms after adsorption, indicating the lowest energy and most stable structure. This was attributed to the low cooperative interaction between the  $\text{La(III)/Ce(III)}$  and  $\text{Mg}$  sites.



**Figure 9.**  $\text{MgO}$  (a),  $\text{MgFe}_2\text{O}_4$  (b) and  $\text{MgFe}_2\text{O}_4/\text{MgO}$  (c) before structural optimization;  $\text{MgFe}_2\text{O}_4/\text{MgO}$  after structural optimization (d); adsorption of  $\text{Ce(III)}$  (e) and  $\text{La(III)}$  (f) by  $\text{MgFe}_2\text{O}_4/\text{MgO}$ ; differential charge density maps of  $\text{Ce(III)}$  (g,h) and  $\text{La(III)}$  (i,j) adsorbed by  $\text{MgFe}_2\text{O}_4/\text{MgO}$ .

Calculating the adsorption energy and ion bond lengths for  $\text{MgFe}_2\text{O}_4/\text{MgO}$  adsorbing  $\text{Ce(III)}$  and  $\text{La(III)}$  allows the analysis of the binding capabilities between the adsorbent and rare earth ions. The calculations revealed that the adsorption energy of  $\text{MgFe}_2\text{O}_4/\text{MgO}$  for  $\text{Ce(III)}$  ( $E_{\text{ads}} = -0.92$  eV) is lower than that of  $\text{La(III)}$  ( $E_{\text{ads}} = -0.80$  eV). Additionally, the  $\text{Ce-O}$  bond length ( $2.322$  Å) is shorter than the  $\text{La-O}$  bond length ( $2.805$  Å), indicating a stronger interaction between  $\text{Ce(III)}$  and  $\text{MgFe}_2\text{O}_4/\text{MgO}$  compared with  $\text{La(III)}$  [68,69]. Furthermore, adsorption experiments also demonstrate that the maximum adsorption capacity for  $\text{Ce(III)}$  ( $5689.69$  mg/g) exceeds that for  $\text{La(III)}$  ( $2123.50$  mg/g), indicating that  $\text{Ce(III)}$  is more easily removed by  $\text{MgFe}_2\text{O}_4/\text{MgO}$  than  $\text{La(III)}$ . Moreover, the adsorption energies are all less than  $-0.5$  eV, suggesting that the adsorption process is chemical adsorption.

Figure 9g–j illustrate the differential charge density plots for the adsorption configurations of  $\text{Ce(III)}$  and  $\text{La(III)}$ . In these plots, red represents regions of increased charge,

and blue indicates regions of decreased charge. It is evident from the figures that there is charge accumulation between the adsorbed molecules and the surface in both adsorption systems, confirming electronic transfer or sharing between Ce(III), La(III), and MgFe<sub>2</sub>O<sub>4</sub>/MgO. In comparison to La(III), Ce(III) exhibits a more intense charge transfer with MgFe<sub>2</sub>O<sub>4</sub>/MgO, indicating a greater affinity between Ce(III) and MgFe<sub>2</sub>O<sub>4</sub>/MgO. This is in line with the results of bond length calculations, adsorption energy computations, and adsorption experiments.

To delve deeper into the interaction between La(III)/Ce(III) and MgFe<sub>2</sub>O<sub>4</sub>/MgO, the partial densities of states (PDOSs) of Ce(III), La(III), O (oxygen atoms on MgFe<sub>2</sub>O<sub>4</sub>/MgO), and Mg (magnesium atoms on MgFe<sub>2</sub>O<sub>4</sub>/MgO) are presented in Figure 10. The green vertical dashed line represents orbital overlap, the black vertical dashed line denotes the Fermi level, the dashed lines indicate pre-adsorption, and the solid lines represent post-adsorption. After the adsorption of Ce(III) and La(III), the orbitals of the Mg and O atoms to the left of the Fermi level transition to lower energy states, indicating an electron transfer process during adsorption [70].

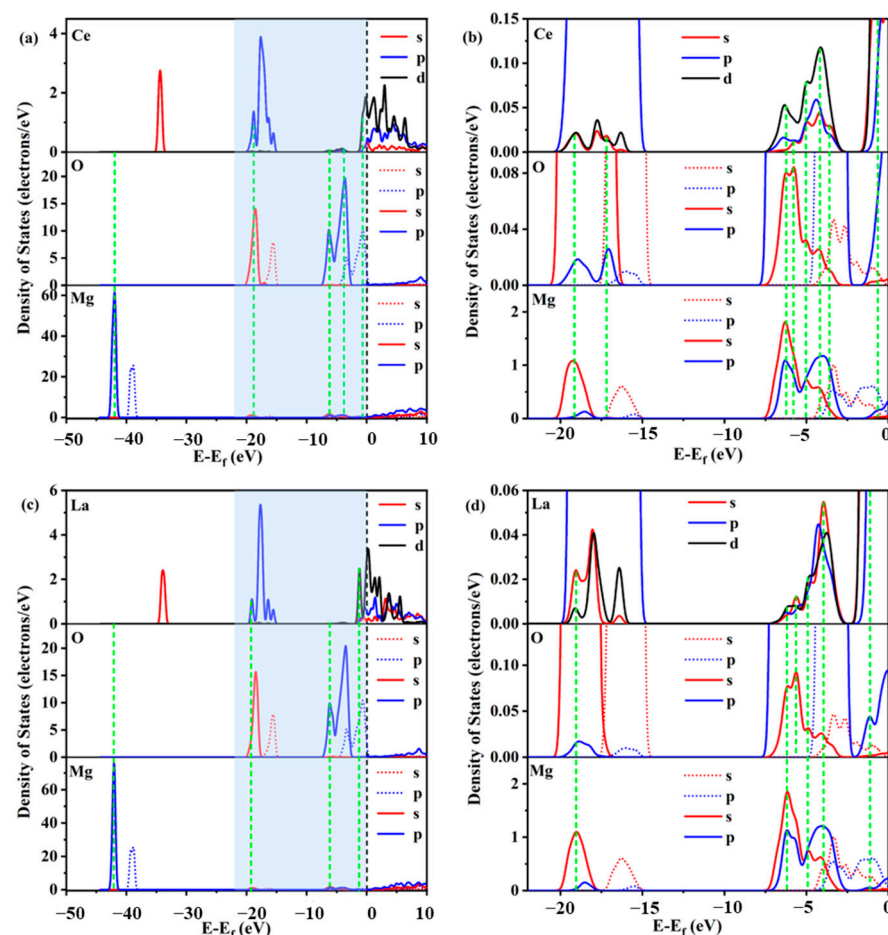


**Figure 10.** (a) PDOS before and after Ce(III) adsorption by MgFe<sub>2</sub>O<sub>4</sub>/MgO; (b) enlarged PDOS before and after Ce(III) adsorption by MgFe<sub>2</sub>O<sub>4</sub>/MgO; (c) PDOS before and after La(III) adsorption by MgFe<sub>2</sub>O<sub>4</sub>/MgO; (d) enlarged PDOS before and after La(III) adsorption by MgFe<sub>2</sub>O<sub>4</sub>/MgO.

The PDOS analysis revealed that Mg p orbitals do not overlap with Ce and La s, p, and d orbitals, suggesting that Mg p orbitals are not involved in the adsorption of Ce and La. Figure 10a,b shows the overlap between the s and p orbitals of the O atoms and Ce s, p, and d orbitals, as well as the overlap between the s orbital of the Mg atoms and the Ce s orbital. This suggests orbital hybridization between MgFe<sub>2</sub>O<sub>4</sub>/MgO and Ce, with strong charge transfer and chemical interactions between Ce and O/Mg atoms. Figure 10c,d shows that the s and p orbitals of the O atoms overlap with the La s, p, and d orbitals,

and the s orbital of the Mg atoms overlaps with the La s orbital. This indicates orbital hybridization between  $\text{MgFe}_2\text{O}_4/\text{MgO}$  and La, accompanied by strong charge transfer and chemical interactions between the La and O/Mg atoms [71]. This aligns with the previously discussed adsorption mechanisms of  $\text{MgFe}_2\text{O}_4/\text{MgO}$  for Ce(III) and La(III). Furthermore, a comparison of the adsorption results between Ce(III)/La(III) and  $\text{MgFe}_2\text{O}_4/\text{MgO}$  reveals that the overlap between the Ce and  $\text{MgFe}_2\text{O}_4/\text{MgO}$  orbitals is greater than that between the La and  $\text{MgFe}_2\text{O}_4/\text{MgO}$  orbitals. This indicates stronger orbital hybridization and electron transfer between Ce and  $\text{MgFe}_2\text{O}_4/\text{MgO}$  compared to La and  $\text{MgFe}_2\text{O}_4/\text{MgO}$ . Consequently, the adsorption capacity of  $\text{MgFe}_2\text{O}_4/\text{MgO}$  for Ce(III) is higher than that for La(III).

### 3.8. Cycling Performance

Aside from possessing a high adsorption capacity, a good adsorbent should also exhibit excellent regeneration and reusability. Using a 0.1 M HCl solution as the desorption solution effectively extracted Ce and La from the HOM-m  $\text{MgFe}_2\text{O}_4/\text{MgO}$ . The recyclability of HOM-m  $\text{MgFe}_2\text{O}_4/\text{MgO}$  was evaluated through three consecutive adsorption–desorption cycles, as depicted in Figure S1. After three consecutive cycles, the removal efficiency of HOM-m  $\text{MgFe}_2\text{O}_4/\text{MgO}$  for Ce(III) and La(III) decreased slightly but remained above 60%. This indicates that the prepared HOM-m  $\text{MgFe}_2\text{O}_4/\text{MgO}$  is an efficient and high-performance recyclable adsorbent for Ce(III) and La(III).

## 4. Conclusions

In this study, a hierarchical or ordered magnetic  $\text{MgFe}_2\text{O}_4/\text{MgO}$  adsorbent with macroporous and mesoporous structures was prepared using a template method for efficient adsorption of Ce (III) and La (III). The maximum adsorption capacity of La (III) is 2123.50 mg/g, and that of Ce (III) is 5689.69 mg/g. Within a wide pH range of 5–9, the adsorbent exhibits higher adsorption capacity for La (III) and Ce (III). The adsorption of Ce (III) and La (III) by HOM-m  $\text{MgFe}_2\text{O}_4/\text{MgO}$  follows the Freundlich isothermal adsorption model and the pseudo-second-order kinetic model, manifesting as a non-uniform multi-step adsorption process dominated by chemisorption. Moreover, the adsorption is endothermic and spontaneous. DFT calculations indicate that the adsorption process is driven by the interaction between Ce (III) and La (III) ions and oxygen atoms on the  $\text{MgO}$  surface. Among them,  $\text{MgFe}_2\text{O}_4/\text{MgO}$  has a higher affinity for Ce (III) than La (III) and a stronger adsorption effect. Adsorbents exhibit superparamagnetism and can be efficiently and quickly separated from aqueous solutions using magnets. After three consecutive adsorption desorption processes, the adsorbent still maintains a good adsorption effect on La (III) and Ce (III). HOM-m  $\text{MgFe}_2\text{O}_4/\text{MgO}$  has a high adsorption capacity, fast adsorption rate, low recovery cost, and good cycling stability for Ce (III) and La (III). It is a promising and efficient rare earth element capture agent, which is of great significance for the effective management of water resources in rare earth mining areas.

**Supplementary Materials:** The following supporting information can be downloaded at <https://www.mdpi.com/article/10.3390/separations11120333/s1>, Text S1. Preparation of polystyrene colloidal crystal template; Text S2. Calculation methods for pore size, pore volume, and specific surface area; Figure S1: The removal rate for La(III) and Ce(III) as a function of adsorption–desorption cycles; Table S1: Supplier, mass fraction purity, and CAS registry number of chemicals; Table S2: Equations and parameters used in kinetics and isotherm models; Table S3: Pseudo-first-order kinetic model correlation coefficients of the adsorption of Ce(III) and La(III) by HOM-m  $\text{MgFe}_2\text{O}_4/\text{MgO}$ ; Table S4: Pseudo-second-order kinetic model correlation coefficients of the adsorption of Ce(III) and La(III) by HOM-m  $\text{MgFe}_2\text{O}_4/\text{MgO}$ ; Table S5: Intra-particle diffusion model correlation coefficients of the adsorption of Ce(III) and La(III) by HOM-m  $\text{MgFe}_2\text{O}_4/\text{MgO}$ ; Table S6: Adsorption isotherm parameters for Ce(III) and La(III) adsorption on HOM-m  $\text{MgFe}_2\text{O}_4/\text{MgO}$ ; Table S7: Thermodynamic parameters for Ce(III) and La(III) removal by HOM-m  $\text{MgFe}_2\text{O}_4/\text{MgO}$ ; Table S8: The content of XPS elements on the surface of the sample before and after the adsorption of Ce(III) and La(III) by adsorbents.

**Author Contributions:** Conceptualization, L.Z.; Writing—review & editing, L.Z., B.L.; Writing—original draft, J.L.; Data curation, J.L.; Funding acquisition, B.L. All authors have read and agreed to the published version of the manuscript.

**Funding:** This work was supported by the Natural Science Foundation of Jiangxi Province (20202BABL204033), Program for Excellent Young Talents, JXUST (2019006). The funders of the above two fundings are both Baixiong Liu.

**Data Availability Statement:** Data are contained within the article or Supplementary Materials.

**Conflicts of Interest:** The authors declare no conflicts of interest.

## References

1. Ni, S.; Chen, Q.; Gao, Y.; Guo, X.; Sun, X. Recovery of rare earths from industrial wastewater using extraction-precipitation strategy for resource and environmental concerns. *Miner. Eng.* **2020**, *151*, 106315. [[CrossRef](#)]
2. Huang, C.; Wang, Y.; Huang, B.; Dong, Y.; Sun, X. The recovery of rare earth elements from coal combustion products by ionic liquids. *Miner. Eng.* **2019**, *130*, 142–147. [[CrossRef](#)]
3. Yu, J.M.; Luo, D.; Ma, Z.J.; Zheng, B.; Cheng, F.F.; Xiong, W.W. Effective enrichment of low-concentration rare-earth ions by three-dimensional thiostannate  $K_2Sn_2S_5$ . *ACS Appl. Mater. Interfaces* **2021**, *13*, 55188–55197. [[CrossRef](#)] [[PubMed](#)]
4. Wang, J.; Zhang, J.; Ni, S.; Xing, H.; Meng, Q.; Bian, Y.; Yang, L. Cation-Intercalated Lamellar  $MoS_2$  Adsorbent Enables Highly Selective Capture of Cesium. *ACS Appl. Mater. Interfaces* **2023**, *15*, 49095–49106. [[CrossRef](#)]
5. Dutta, T.; Kim, K.H.; Uchimiya, M.; Kwon, E.E.; Jeon, B.H.; Deep, A.; Yun, S.T. Global demand for rare earth resources and strategies for green mining. *Environ. Res.* **2016**, *150*, 182–190. [[CrossRef](#)]
6. Luo, X.; Zhang, Y.; Zhou, H.; He, K.; Luo, C.; Liu, Z.; Tang, X. Review on the development and utilization of ionic rare earth ore. *Minerals* **2022**, *12*, 554. [[CrossRef](#)]
7. Huang, X.W.; Long, Z.Q.; Wang, L.S.; Feng, Z.Y. Technology development for rare earth cleaner hydrometallurgy in China. *Rare Met.* **2015**, *34*, 215–222. [[CrossRef](#)]
8. Yang, X.J.; Lin, A.; Li, X.L.; Wu, Y.; Zhou, W.; Chen, Z. China's ion-adsorption rare earth resources, mining consequences and preservation. *Environ. Dev.* **2013**, *8*, 131–136. [[CrossRef](#)]
9. Chen, Z.; Sang, F.; Xu, J.; Luo, G.; Wang, Y. Efficient enrichment and recovery of rare earth elements with low concentration by membrane dispersion micro-extractors. *Chem. Eng. Process* **2018**, *127*, 127–135. [[CrossRef](#)]
10. Royer-Lavallée, A.; Neculita, C.M.; Coudert, L. Removal and potential recovery of rare earth elements from mine water. *J. Ind. Eng. Chem.* **2020**, *89*, 47–57. [[CrossRef](#)]
11. Brewer, A.; Dror, I.; Berkowitz, B. Electronic waste as a source of rare earth element pollution: Leaching, transport in porous media, and the effects of nanoparticles. *Chemosphere* **2022**, *287*, 132217. [[CrossRef](#)] [[PubMed](#)]
12. Chen, H.; Chen, Z.; Chen, H. Impacts of Ion Adsorption Type Rare Earth Mining Techniques on Topsoil in Mining Area. *Pol. J. Environ. Stud.* **2024**, *33*, 1585–1594. [[CrossRef](#)]
13. Cheng, Y.; Zhang, T.; Zhang, L.; Ke, Z.; Kovarik, L.; Dong, H. Resource recovery: Adsorption and biomineralization of cerium by *Bacillus licheniformis*. *J. Hazard. Mater.* **2022**, *426*, 127844. [[CrossRef](#)] [[PubMed](#)]
14. Kyra, C.P.; Joshua, S.; Mark, P.S. New insights into rare earth element (REE) particulate generated by cigarette lighters: An electron microscopy and materials science investigation of a poorly understood indoor air pollutant and constraints for urban geochemistry. *Environ. Earth Sci.* **2017**, *76*, 369. [[CrossRef](#)]
15. Golroudbary, S.R.; Makarava, I.; Kraslawski, A. Global environmental cost of using rare earth elements in green energy technologies. *Sci. Total Environ.* **2022**, *832*, 155022. [[CrossRef](#)]
16. Hossain, M.K.; Ahmed, M.H.; Khan, M.I.; Miah, M.S.; Hossain, S. Recent Progress of Rare Earth Oxides for Sensor, Detector, and Electronic Device Applications: A Review. *ACS Appl. Electron. Mater.* **2021**, *3*, 4255–4283. [[CrossRef](#)]
17. Ebrahim, A.; Bahram, R. Removal of cerium from different aqueous solutions using different adsorbents: A review. *Process Saf. Environ. Prot.* **2019**, *124*, 345–362. [[CrossRef](#)]
18. Sidra, I.; Deepika, L.R.; Varsha, S.; Muhammad, B.A.; Mika, S. Understanding the factors affecting the adsorption of Lanthanum using different adsorbents: A critical review. *Chemosphere* **2018**, *204*, 413–430. [[CrossRef](#)]
19. Sordyl, J.; Staszal, K.; Leś, M.; Manecki, M. Removal of REE and Th from solution by co-precipitation with Pb-phosphates. *Appl. Geochem.* **2023**, *158*, 105780. [[CrossRef](#)]
20. Bashiri, A.; Nikzad, A.; Maleki, R.; Asadnia, M.; Razmjou, A. Rare earth elements recovery using selective membranes via extraction and rejection. *Membranes* **2022**, *12*, 80. [[CrossRef](#)]
21. Artiushenko, O.; da Silva, R.F.; Zaitsev, V. Recent advances in functional materials for rare earth recovery: A review. *Sustain. Mater. Technol.* **2023**, *37*, e00681. [[CrossRef](#)]
22. Rumky, J.; Deb, A.; Ramasamy, D.L.; Sillanpää, M.; Häkkinen, A.; Repo, E. Utilization of sludge-based alginate beads for the application of rare earth elements (REEs) recovery from wastewater: A waste to resource approach. *J. Clean. Prod.* **2022**, *362*, 132496. [[CrossRef](#)]



23. Arunraj, B.; Rajesh, V.; Rajesh, N. Potential application of graphene oxide and *Aspergillus niger* spores with high adsorption capacity for recovery of europium from red phosphor, compact fluorescent lamp and simulated radioactive waste. *J. Rare Earths* **2023**, *41*, 157–166. [[CrossRef](#)]
24. Pinheiro, R.F.; Grimm, A.; Oliveira, M.L.; Vieillard, J.; Silva, L.F.; De Brum, I.A.; dos Reis, G.S. Adsorptive behavior of the rare earth elements Ce and La on a soybean pod derived activated carbon: Application in synthetic solutions, real leachate and mechanistic insights by statistical physics modeling. *Chem. Eng. J.* **2023**, *471*, 144484. [[CrossRef](#)]
25. Lv, Y.; Chen, L.; Zhang, A.; Sheng, G.; Liao, Q. Highly efficient removal of rare earth elements by two-dimensional titanium carbide nanosheets as impacted via water chemistry. *Environ. Sci. Pollut. Res.* **2023**, *30*, 90936–90948. [[CrossRef](#)]
26. Mosai, A.K.; Chimuka, L.; Cukrowska, E.M.; Kotzé, I.A.; Tutu, H. The recovery of rare earth elements (REEs) from aqueous solutions using natural zeolite and bentonite. *Water Air Soil Pollut.* **2019**, *230*, 188. [[CrossRef](#)]
27. Feng, X.; Onel, O.; Council-Troche, M.; MacCormac, B.L.; Noble, A.; Yoon, R.H.; Morris, J.R. Rare earth ion-adsorption clays in the presence of iron at basic pH: Adsorption mechanism and extraction method. *Appl. Clay Sci.* **2023**, *231*, 106744. [[CrossRef](#)]
28. Dalvanda, R.; Kianpourb, E.; Tahzibia, H.; Aziziana, S. MgO nano-sheets for adsorption of anionic dyes from aqueous solution: Equilibrium and kinetics studies. *Surf. Interfaces* **2020**, *21*, 100722. [[CrossRef](#)]
29. Huang, J.; Ling, G.; Wu, Y.; Zhai, J.; Zong, J. Mesoporous Reticular Magnesium Oxide with High Specific Surface Area: Preparation, Characterization, Adsorption Performance and Mechanism for Pb(II) in Wastewater. *Chin. J. Inorg. Chem.* **2020**, *36*, 2031–2040. [[CrossRef](#)]
30. Yan, X.; Tian, Z.; Peng, W.; Zhang, J.; Tong, Y.; Li, J.; Zhang, J. Synthesis of nano-octahedral MgO via a solvothermal-solid-decomposition method for the removal of methyl orange from aqueous solutions. *RSC Adv.* **2020**, *10*, 10681–10688. [[CrossRef](#)]
31. Namvar-Mahboub, M.; Khodeir, E.; Bahadori, M.; Mahdizadeh, S.M. Preparation of magnetic MgO/Fe<sub>3</sub>O<sub>4</sub> via the green method for competitive removal of Pb and Cd from aqueous solution. *Colloids Surf. A* **2020**, *589*, 124419. [[CrossRef](#)]
32. Ghoniem, M.G.; Ben Aissa, M.A.; Ali, F.A.M.; Khairy, M. Efficient and Rapid Removal of Pb (II) and Cu (II) Heavy Metals from Aqueous Solutions by MgO Nanorods. *Inorganics* **2022**, *10*, 256. [[CrossRef](#)]
33. Liu, B.; Li, C.; Zhang, L.; Liu, Z.; Kuang, M.; He, X. Fabrication of three-dimensional ordered macroporous/mesoporous magnesium oxide for efficient cadmium removal. *Ceram. Int.* **2021**, *47*, 22830–22838. [[CrossRef](#)]
34. Zhao, X.; Lv, Y.; Liu, S.; Ren, Y.; Feng, J.; Gao, M.; Fan, Z.; Zhang, Z. Fabrication of mesoporous magnesium oxide nanosheets using magnesium powder and their excellent adsorption of Ni (II). *J. Colloid Interface Sci.* **2018**, *510*, 69–76. [[CrossRef](#)]
35. Yu, X.Y.; Luo, T.; Jia, Y.; Zhang, Y.X.; Liu, J.H.; Huang, X.J. Porous hierarchically micro-/nanostructured MgO: Morphology control and their excellent performance in As (III) and As (V) removal. *J. Phys. Chem. C* **2011**, *115*, 22242–22250. [[CrossRef](#)]
36. Abshirini, Y.; Esmaili, H.; Foroutan, R. Enhancement removal of Cr (VI) ion using magnetically modified MgO nanoparticles. *Mater. Res. Express* **2019**, *6*, 125513. [[CrossRef](#)]
37. Fukushi, K.; Miyashita, S.; Kasama, T.; Takahashi, Y.; Morodome, S. Superior removal of selenite by periclase during transformation to brucite under high-pH conditions. *J. Hazard. Mater.* **2019**, *371*, 370–380. [[CrossRef](#)]
38. Cui, W.; Li, P.; Wang, Z.; Zheng, S.; Zhang, Y. Adsorption study of selenium ions from aqueous solutions using MgO nanosheets synthesized by ultrasonic method. *J. Hazard. Mater.* **2018**, *341*, 268–276. [[CrossRef](#)]
39. Yang, W.; Hu, W.; Zhang, J.; Wang, W.; Cai, R.; Pan, M.; Zeng, H. Tannic acid/Fe<sup>3+</sup> functionalized magnetic graphene oxide nanocomposite with high loading of silver nanoparticles as ultra-efficient catalyst and disinfectant for wastewater treatment. *Chem. Eng. J.* **2021**, *405*, 126629. [[CrossRef](#)]
40. He, X.; Ma, C.; Wang, Z.; Zhang, M. Construction of Shape-Controlled MgO Microstructures by Natural Bischofite for Cost-Efficient Dye Adsorption. *Chemistryselect* **2023**, *8*, e202203701. [[CrossRef](#)]
41. Liu, Z.; Li, C.; Kuang, M.; Liu, B.; Yang, B. Template synthesis of ordered mesoporous MgO with superior adsorption for Pb (II) and Cd (II). *Environ. Sci. Pollut. Res.* **2021**, *28*, 31630–31639. [[CrossRef](#)] [[PubMed](#)]
42. Ashour, R.M.; Abdelhamid, H.N.; Abdel-Magied, A.F.; Abdel-Khalek, A.A.; Ali, M.M.; Uheida, A.; Dutta, J. Rare earth ions adsorption onto graphene oxide nanosheets. *Solvent Extr. Ion Exch.* **2017**, *35*, 91–103. [[CrossRef](#)]
43. Crane, R.A.; Sapsford, D.J. Sorption and fractionation of rare earth element ions onto nanoscale zerovalent iron particles. *Chem. Eng. J.* **2018**, *345*, 126–137. [[CrossRef](#)]
44. Wang, L.; Wang, J.; He, C.; Lyu, W.; Zhang, W.; Yan, W.; Yang, L. Development of rare earth element doped magnetic biochars with enhanced phosphate adsorption performance. *Colloids Surf. A* **2019**, *561*, 236–243. [[CrossRef](#)]
45. Kegl, T.; Ban, I.; Lobnik, A.; Košak, A. Synthesis and characterization of novel  $\gamma$ -Fe<sub>2</sub>O<sub>3</sub>-NH<sub>4</sub>OH@ SiO<sub>2</sub> (APTMS) nanoparticles for dysprosium adsorption. *J. Hazard. Mater.* **2019**, *378*, 120764. [[CrossRef](#)]
46. Asadi, R.; Abdollahi, H.; Boroumand, Z.; Kisomi, A.S.; Darvanjooghi, M.H.K.; Magdouli, S.; Brar, S.K. Intelligent modelling for the elimination of lanthanides (La<sup>3+</sup>, Ce<sup>3+</sup>, Nd<sup>3+</sup> and Eu<sup>3+</sup>) from aqueous solution by magnetic CoFe<sub>2</sub>O<sub>4</sub> and CoFe<sub>2</sub>O<sub>4</sub>-GO spinel ferrite nanocomposites. *Environ. Pollut.* **2022**, *309*, 119770. [[CrossRef](#)]
47. Allwin Mages Raj, A.F.P.; Bauman, M.; Dimitrušev, N.; Ali, L.M.; Onofre, M.; Gary-Bobo, M.; Košak, A. Superparamagnetic Spinel-Ferrite Nano-Adsorbents Adapted for Hg<sup>2+</sup>, Dy<sup>3+</sup>, Tb<sup>3+</sup> Removal/Recycling: Synthesis, Characterization, and Assessment of Toxicity. *Int. J. Mol. Sci.* **2023**, *24*, 10072. [[CrossRef](#)]
48. Gu, W.; Li, X.; Xing, M.; Fang, W.; Wu, D. Removal of phosphate from water by amine-functionalized copper ferrite chelated with La (III). *Sci. Total Environ.* **2018**, *619*, 42–48. [[CrossRef](#)]



49. Sun, Z.H.; Li, J.; Wang, X.J.; Zhang, Y.N.; Xi, S.Q. MgFe<sub>2</sub>O<sub>4</sub>/MgO modified biochar with oxygen vacancy and surface hydroxyl groups for enhanced peroxymonosulfate activation to remove sulfamethoxazole through singlet oxygen-dominated nonradical oxidation process. *Chem. Eng. J.* **2023**, *477*, 146960. [[CrossRef](#)]
50. He, X.Y.; Lu, J.R.; Wei, H.; Liu, B.X. Macroporous honeycomb-like magnesium oxide fabricated as long-life and outstanding Pb(II) adsorbents combined with mechanism insight. *Environ. Sci. Pollut. Res.* **2023**, *30*, 38380–38393. [[CrossRef](#)]
51. Khot, V.M.; Salunkhe, A.B.; Phadatar, M.R.; Pawar, S.H. Formation, microstructure and magnetic properties of nanocrystalline MgFe<sub>2</sub>O<sub>4</sub>. *Environ. Mater. Chem. Phys.* **2012**, *132*, 2–3. [[CrossRef](#)]
52. Vikash, K.T.; Rajamani, N. Magnetically separable, bifunctional catalyst MgFe<sub>2</sub>O<sub>4</sub> obtained by epoxide mediated synthesis. *Adv. Powder Technol.* **2016**, *27*, 4. [[CrossRef](#)]
53. Cai, Y.C.; Li, C.L.; Wu, D.; Wang, W.; Tan, F.T.; Wang, X.Y.; Wong, P.K.; Qiao, X.L. Highly active MgO nanoparticles for simultaneous bacterial inactivation and heavy metal removal from aqueous solution. *Chem. Eng. J.* **2016**, *312*, 15. [[CrossRef](#)]
54. Xiong, C.M.; Wang, W.; Tan, F.T.; Luo, F.; Chen, J.G.; Qiao, X.L. Investigation on the efficiency and mechanism of Cd(II) and Pb(II) removal from aqueous solutions using MgO nanoparticles. *J. Hazard. Mater.* **2015**, *299*, 15. [[CrossRef](#)] [[PubMed](#)]
55. Sharma, R.; Thakur, P.; Sharma, P.; Sharma, V. Ferrimagnetic Ni<sup>2+</sup> doped Mg-Zn spinel ferrite nanoparticles for high density information storage. *J. Alloys Compd.* **2017**, *704*, 7–17. [[CrossRef](#)]
56. Liu, L.; Yue, T.; Liu, R.; Lin, H.; Wang, D.; Li, B. Efficient absorptive removal of Cd (II) in aqueous solution by biochar derived from sewage sludge and calcium sulfate. *Bioresour. Technol.* **2021**, *336*, 125333. [[CrossRef](#)]
57. Wan, S.; Qiu, L.; Tang, G.; Chen, W.; Li, Y.; Gao, B.; He, F. Ultrafast sequestration of cadmium and lead from water by manganese oxide supported on a macro-mesoporous biochar. *Chem. Eng. J.* **2020**, *387*, 124095. [[CrossRef](#)]
58. Yin, G.; Chen, X.; Sarkar, B.; Bolan, N.S.; Wei, T.; Zhou, H.; Wang, H. Co-adsorption mechanisms of Cd (II) and As (III) by an Fe-Mn binary oxide biochar in aqueous solution. *Chem. Eng. J.* **2023**, *466*, 143199. [[CrossRef](#)]
59. Dim, P.E.; Mustapha, L.S.; Termatanun, M.; Okafor, J.O. Adsorption of chromium (VI) and iron (III) ions onto acid-modified kaolinite: Isotherm, kinetics and thermodynamics studies. *Arab. J. Chem.* **2021**, *14*, 103064. [[CrossRef](#)]
60. Xu, C.; Shi, S.; Wang, X.; Zhou, H.; Wang, L.; Zhu, L.; Xu, D. Electrospun SiO<sub>2</sub>-MgO hybrid fibers for heavy metal removal: Characterization and adsorption study of Pb (II) and Cu (II). *J. Hazard. Mater.* **2020**, *381*, 120974. [[CrossRef](#)]
61. Kumar, S.; Nair, R.R.; Pillai, P.B.; Gupta, S.N.; Iyengar, M.A.R.; Sood, A.K. Graphene oxide-MnFe<sub>2</sub>O<sub>4</sub> magnetic nanohybrids for efficient removal of lead and arsenic from water. *ACS Appl. Mater. Interfaces* **2014**, *6*, 17426–17436. [[CrossRef](#)] [[PubMed](#)]
62. Ling, L.L.; Liu, W.J.; Zhang, S.; Jiang, H. Magnesium oxide embedded nitrogen self-doped biochar composites: Fast and high-efficiency adsorption of heavy metals in an aqueous solution. *Environ. Sci. Technol.* **2017**, *51*, 10081–10089. [[CrossRef](#)] [[PubMed](#)]
63. Wu, J.; Wang, T.; Wang, J.; Zhang, Y.; Pan, W.P. A novel modified method for the efficient removal of Pb and Cd from wastewater by biochar: Enhanced the ion exchange and precipitation capacity. *Sci. Total Environ.* **2021**, *754*, 142150. [[CrossRef](#)] [[PubMed](#)]
64. Marwani, H.M.; Bakhsh, E.M.; Khan, S.B.; Danish, E.Y.; Asiri, A.M. Cerium oxide-cadmium oxide nanomaterial as efficient extractant for yttrium ions. *J. Mol. Liq.* **2018**, *269*, 252–259. [[CrossRef](#)]
65. Li, S.; Huang, X.; Wan, Z.; Liu, J.; Lu, L.; Peng, K.; Bhattarai, R. Green synthesis of ultrapure La(OH)<sub>3</sub> nanoparticles by one-step method through spark ablation and electrospinning and its application to phosphate removal. *Chem. Eng. J.* **2020**, *388*, 124373. [[CrossRef](#)]
66. Chen, Y.; Ai, X.; Huang, B.; Huang, M.; Huang, Y.; Lu, Y. Consecutive preparation of hydrochar catalyst functionalized in situ with sulfonic groups for efficient cellulose hydrolysis. *Cellulose* **2017**, *24*, 2743–2752. [[CrossRef](#)]
67. Cui, G.; Liu, M.; Chen, Y.; Zhang, W.; Zhao, J. Synthesis of a ferric hydroxide-coated cellulose nanofiber hybrid for effective removal of phosphate from wastewater. *Carbohydr. Polym.* **2016**, *154*, 40–47. [[CrossRef](#)]
68. O'Connor, N.J.; Jonayat, A.S.M.; Janik, M.J.; Senftle, T.P. Interaction trends between single metal atoms and oxide supports identified with density functional theory and statistical learning. *Nat. Catal.* **2018**, *1*, 531–539. [[CrossRef](#)]
69. Xu, L.; Liu, Y.; Wang, J.; Tang, Y.; Zhang, Z. Selective adsorption of Pb<sup>2+</sup> and Cu<sup>2+</sup> on amino-modified attapulgite: Kinetic, thermal dynamic and DFT studies. *J. Hazard. Mater.* **2021**, *404*, 124140. [[CrossRef](#)]
70. Chen, Q.; Tang, Z.; Li, H.; Wu, M.; Zhao, Q.; Pan, B. An electron-scale comparative study on the adsorption of six divalent heavy metal cations on MnFe<sub>2</sub>O<sub>4</sub>@CAC hybrid: Experimental and DFT investigations. *Chem. Eng. J.* **2020**, *381*, 122656. [[CrossRef](#)]
71. Feng, Z.; Chen, N.; Liu, T.; Feng, C. KHCO<sub>3</sub> activated biochar supporting MgO for Pb (II) and Cd (II) adsorption from water: Experimental study and DFT calculation analysis. *J. Hazard. Mater.* **2022**, *426*, 128059. [[CrossRef](#)] [[PubMed](#)]

**Disclaimer/Publisher's Note:** The statements, opinions and data contained in all publications are solely those of the individual author(s) and contributor(s) and not of MDPI and/or the editor(s). MDPI and/or the editor(s) disclaim responsibility for any injury to people or property resulting from any ideas, methods, instructions or products referred to in the content.